Robust Method for 3D Arterial Spin Labeling in Mice

Brige Paul Chugh,[1,2]* Jonathan Bishop,[1] Yu-Qing Zhou,[1] Jian Wu,[1,3] R. Mark Henkelman,[1,2] and John G. Sled[1,2]

Arterial spin labeling is a versatile perfusion quantification methodology, which has the potential to provide accurate characterization of cerebral blood flow (CBF) in mouse models. However, a paucity of physiological data needed for accurate modeling, more stringent requirements for gradient performance, and strong artifacts introduced by magnetization transfer present special challenges for accurate CBF mapping in the mouse. This article describes robust mapping of CBF over three-dimensional brain regions using amplitude-modulated continuous arterial spin labeling. To provide physiological data for CBF modeling, the carotid artery blood velocity distribution was characterized using pulsed-wave Doppler ultrasound. These blood velocity measurements were used in simulations that optimize inversion efficiency for parameters meeting MRI gradient duty cycle constraints. A rapid slice positioning algorithm was developed and evaluated to provide accurate positioning of the labeling plane. To account for enhancement of T_1 due to magnetization transfer, a binary spin bath model of magnetization transfer was used to provide a more accurate estimate of CBF. Finally, a study of CBF was conducted on 10 mice with findings of highly reproducible inversion efficiency (mean ± standard-error-of-the-mean, 0.67 ± 0.03), statistically significant variation in CBF over 12 brain regions ($P < 0.0001$) and a mean ± standard-error-of-the-mean whole brain CBF of 219 ± 6 mL/100 g/min. Magn Reson Med 68:98–106, 2012.

Key words: arterial spin labeling; cerebral blood flow; mouse

Arterial spin labeling (ASL) provides a means for quantifying cerebral blood flow (CBF) over mouse brain regions in a noninvasive manner. Mouse ASL permits longitudinal screening of cerebrovascular phenotypes during the mouse lifespan of 2–3 years, which facilitates the study of vascular factors in disease. Recent ASL applications in mice include models of stroke (1), cerebral malaria (2), sickle cell disease (3), and Alzheimer's disease (4). There is also considerable interest in quantifying CBF in mice for studying blood flow regulatory mechanisms (5) and for the development of disease-specific therapies. The use of ASL in mice is generally motivated by a desire to better understand mouse models of human disease.

Design of robust mouse ASL involves producing images with high enough resolution and signal-to-noise-ratio (SNR) to detect important changes in regional CBF, while meeting experimental constraints of scan time and sample size. The limits on available signal strength and gradient performance as well as physiological differences between the species prevent a simple scaling down of human imaging protocols for ASL from achieving satisfactory results.

Adapting amplitude-modulated continuous ASL (am-CASL) to brain size and carotid blood velocity of mice requires optimization of the labeling gradient and B_1 waveform within the given hardware constraints. Previous work using simulation has shown that, for some combinations of labeling parameters, inversion efficiency with am-CASL may be unstable with respect to small variations in blood velocity (6). It is therefore necessary to map the stable regime to bracket the anticipated blood velocity distribution for the mouse. All ASL pulse sequences are designed to equalize magnetization transfer (MT) signal loss in label and control images. The control experiment in am-CASL uses a radiofrequency pulse, which is sinusoidally modulated at frequency (f_m) to cause arterial spins to doubly invert as they flow through two closely spaced inversion planes. The power and center frequency of the radiofrequency pulse in this control experiment are matched to those used for single inversion, thereby equalizing MT effects on brain tissue. To achieve optimal inversion efficiency, the adiabatic inversion inequalities must be fulfilled, namely, $1/T_{2b} \ll Gv/B_1 \ll \gamma B_1$, where v is the speed of the inflowing spins, G is the strength of the MRI gradient during labeling, B_1 is the amplitude of the radiofrequency field, and T_{2b} is the transverse relaxation time of blood. It is also necessary to fulfill a condition unique to am-CASL that balances the requirement for stable inversion behavior with minimal relaxation (6), namely: $Gv/B_1 f_m \approx 1$. Even after satisfying these conditions, inversion efficiency in am-CASL remains highly sensitive to velocity (7), which requires careful slice positioning to reduce variability in CBF. With mice smaller than humans by a factor of 15 in each linear dimension, it is not possible to obtain high quality localizers rapidly enough to enable accurate slice positioning by eye. Another relevant constraint is the small size of the mouse brain as, for commonly realizable gradient strengths, the 1–2-cm offset from the labeling plane intersecting the common carotid artery to the caudal or rostral limits of the mouse brain corresponds to an off-resonance frequency range of 5–20 kHz. The associated large enhancement of T_1 relaxation due to MT (8), which has been characterized for typical CASL parameters at 7 T in rat (9), must be accounted for in CBF modeling equations to obtain accurate CBF maps (10). Moreover, the equilibrium magnetization of the tissue is reduced by MT. Thus, the constraints of mouse brain size and blood velocity necessitate judicious selection of am-CASL parameters.

[1]Mouse Imaging Centre, The Hospital for Sick Children, Toronto, Ontario, Canada.
[2]Department of Medical Biophysics, University of Toronto, Toronto, Ontario, Canada.
[3]Shanghai Institute of Cardiovascular Diseases, Zhongshan Hospital and Institutes of Biomedical Sciences, Fudan University, Shanghai, China.
*Correspondence to: Brige Paul Chugh, MSc, The Hospital for Sick Children, 25 Orde Street, Toronto, Ontario, Canada M5T 3H7. E-mail: brige@phenogenomics.ca
Received 6 May 2011; revised 15 August 2011; accepted 16 August 2011.
DOI 10.1002/mrm.23209
Published online 18 November 2011 in Wiley Online Library (wileyonlinelibrary.com).

This article describes an experimental approach to implement mouse am-CASL in a robust manner. A rapid slice positioning algorithm is developed to improve the consistency of labeling plane placement and thereby inversion efficiency. Errors in positioning the inversion plane are evaluated. For the purpose of optimizing inversion efficiency parameters, blood velocity distributions in the mouse common carotid arteries are characterized using pulsed-wave Doppler ultrasound. These blood velocity data are used for simulations of inversion efficiency, while satisfying gradient duty cycle and specific absorption rate (SAR) constraints. The sensitivity of inversion efficiency to velocity is determined. Following these developments, three-dimensional (3D) am-CASL is implemented. The final stage of this method is to calculate CBF based on an MT-corrected model applicable to the high CBF values of mice.

MATERIALS AND METHODS

All animal procedures described in this article were approved by the Hospital for Sick Children Animal Care Committee, subject to the Canadian Council for Animal Care.

Development of a Rapid Slice Positioning Algorithm

A slice positioning algorithm was developed that takes advantage of the conspicuity of vessel bifurcations in rapidly acquired MRI localizer images that provide inflow contrast due to short pulse repetition time (TR). By identifying the corresponding vessel bifurcations in a reference 3D vascular image, the prescribed inversion plane can be mapped by landmark registration to the correct position in the in vivo MRI coordinate system. In particular, four easily recognizable vessel landmarks with low positional variability can be identified in midsagittal brain slices (as shown in Fig. 1a).

An MRI anatomical brain atlas was used as a reference coordinate system, with 62 labeled 3D regions (11), prepared by averaging 20 female and 20 male C57BL/6 brain MRI images of 32-μm isotropic resolution (12). The MRI anatomical brain atlas can be accessed at http://www.mouseimaging.ca/technologies/C57Bl6j_mouse_atlas.html.

In this reference coordinate system, the coordinates of these four vessel landmarks were identified using nine postmortem micro-CT images of the cerebral vasculature of C57BL/6 mice that had previously been coregistered to an MRI anatomical brain atlas for blood volume measurements (13). Mean and standard deviation (SD) of each vessel landmark were calculated for the nine brains.

In a postmortem micro-CT cerebral vasculature specimen (13), serving as the reference 3D vascular image, the centerlines of the common carotid arteries were traced using custom-written software. Based on the image intensity gradient along rays perpendicular to the vessel centerline, this software maintains equal distance from the lumen wall (14). The plane perpendicular to the common carotid artery was selected as the inversion plane.

The anatomical brain atlas is oriented so that the $+x$ direction points from medial to right lateral, the $+y$ direction points from caudal to rostral, and the $+z$ direction points from ventral to dorsal. In this coordinate system, in millimeter units, the inversion plane is centered

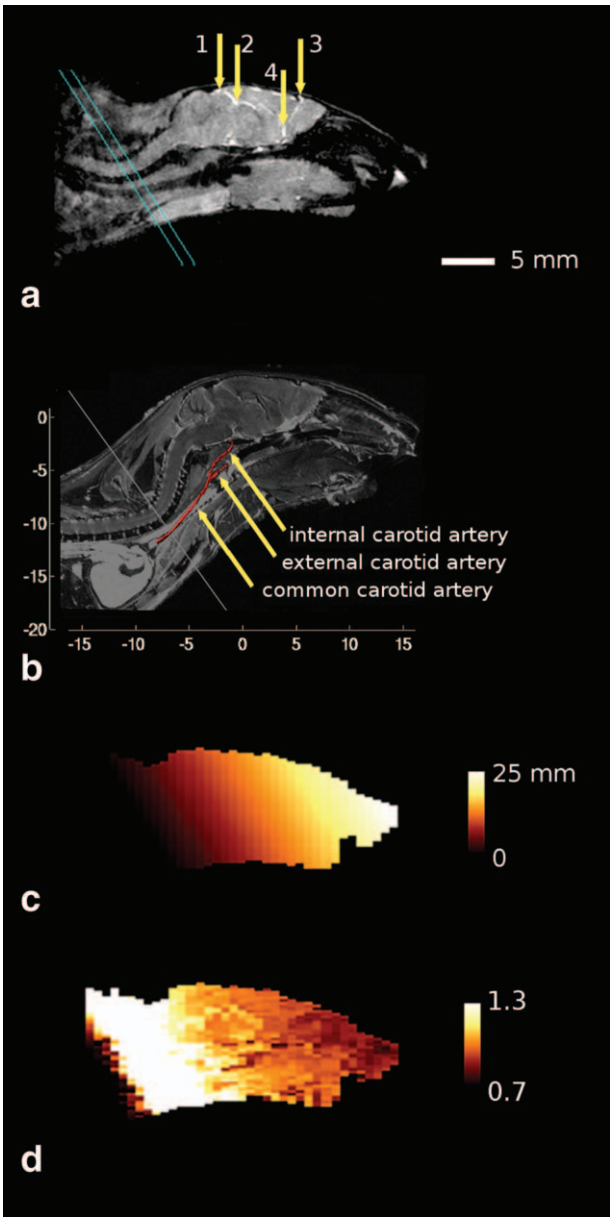

FIG. 1. Illustration of process of correcting for MT starting with an in vivo midsagittal localizer (**a**) with localized vascular landmarks (1, confluence of transverse and superior sagittal sinuses; 2, confluence of anterior cerebral artery and great cerebral vein of Galen; 3, confluence of rostral rhinal veins and superior sagittal sinus; and 4, confluence of medial orbitofrontal artery and azygos of the anterior cerebral artery) and calculated position of inversion slice (slanted blue lines). For illustration purposes, the common carotid artery including its bifurcation is shown overlaid on the midsagittal plane (**b**) of the MR image of a fixed mouse (posture is not identical between **a** and **b**). Also shown is the calculated position and orientation of the labeling plane. The midsagittal slice through the map of computed distance from the inversion slice is shown in (**c**) and the calculated ratio of CBF (post-MT correction) to CBF (pre-MT correction) is shown in (**d**). Note the systematic variation of the MT effect across the brain, decreasing from the caudal to the rostral direction.

midway between the arteries at $C = [0.0, -7.0, -11.3]$ with normal vector of $N = [0.0, 0.80, 0.60]$, as shown in Fig. 1b. Thus, from C and N, it follows that the equation of the inversion plane is $4y + 3z + 61.9 = 0$. The slanted blue lines in Fig. 1a represent the components of an am-CASL double inversion, which are equidistant and symmetric to this calculated inversion plane.

Given the in vivo locations of the landmarks (as described in the "Implementation of am-CASL in Mice" section), the in vivo position of the inversion plane was calculated by rigid body vascular landmark registration using a Procrustes matching algorithm without scaling (15). This algorithm calculates the rigid body transformation that best matches each landmark position in the reference micro-CT image to the corresponding in vivo MRI landmarks. Using this algorithm and reference data, the placement of the labeling plane can be computed rapidly and largely automatically by the operator at the MRI console.

Analysis of Errors in Inversion Plane Positioning

A simulation was conducted to determine the extent to which uncertainty in vascular landmark placement led to errors in inversion plane position. Ten thousand coordinates centered on the true position of each vascular landmark were randomly generated (normal distribution with SD 1 mm, which is the thickness of the MRI localizer scans). The rigid body transformation that maps each simulated coordinate to the true position was computed by the Procrustes matching algorithm without scaling. The inversion plane was transformed accordingly. Mean positional and angular shifts of the inversion plane were determined.

Optimization of Spin Inversion Efficiency Parameters

The time evolution of inflowing blood magnetization was simulated in the mouse common carotid artery. The time–velocity profile of blood was measured in the common carotid, internal carotid, and vertebral arteries of five C57BL/6 mice (body weight 20–25 g) using a Vevo 2100 ultrasound scanner (VisualSonics, Toronto, Canada) equipped with a 40-MHz linear array transducer. 2D Doppler color flow imaging was used to guide each pulse wave Doppler recording in which the intercept angle between the blood flow direction and the ultrasound beam was minimized to under 60° by optimizing transducer orientation. Beam angle was accounted for in the data analysis (16).

Inversion efficiency of am-CASL, namely $(M_{\mathrm{Control}} - M_{\mathrm{Label}})/2M_0$, was calculated in a representative blood velocity distribution for the common carotid artery (spanning four cardiac cycles). The Bloch equations were solved (Runge-Kutta ODE solver, Matlab, The MathWorks Inc., Natick, MA) for a range of velocities (1–40 cm/s) assuming a 3.1-s label pulse with $T_{2b} = 0.25$ s (17) and labeling gradient $G = 13$ mTm^{-1} (constrained by maximum gradient amplitude output at 50% duty cycle). T_1 effects were neglected from the simulation. The simulations were conducted with B_1 varying over the range 1–20 μT and modulation frequency, f_m, varying from 50 to 1000 Hz. Inversion efficiency was calculated as an average over phase (0–π) of the amplitude modulation at the time the spins cross the center of the labeling plane. For each combination of parameters, inversion efficiency was weighted by the blood velocity distribution to provide velocity-weighted inversion efficiency.

The bias of inversion efficiency to inaccurate inversion plane orientation was evaluated by calculating the reduction in velocity-weighted inversion efficiency corresponding to a scaling of the velocity distribution by $\cos(\theta)$. In this case, θ was the mean angular shift of the inversion plane resulting from errors in landmark identification (as described in the "Analysis of Errors in Inversion Plane Positioning" section).

Implementation of am-CASL in Mice

3D am-CASL was performed on 10 female C57BL/6 mice (20–25 g) by the following protocol: each mouse was scanned using a 7-T MRI scanner (Agilent Technologies, Santa Clara, CA) with a horizontal 30 cm inner diameter bore gradient. The mice were anesthetized with 1.2% isoflurane and maintained at core body temperature of 36.5 ± 0.5°C, while being continuously monitored for respiratory rate, temperature, and heart rate (18).

To identify the vascular landmarks needed for positioning the inversion slice, a midsagittal localizer image was acquired using a spoiled gradient-echo pulse sequence [echo time (TE) = 4 ms, TR = 100 ms, 128 × 128 matrix, number of excitations (NEX) = 1, 90° gaussian excitation pulse, field of view (FOV) = 30 mm × 30 mm × 1 mm thick, and total scan time = 13 s]. Each of the four vascular landmarks described in the "Development of a Rapid Slice Positioning Algorithm" section could be easily recognized on 1-mm-thick slices.

Before each am-CASL scan, inversion efficiency was measured with inversion and imaging planes positioned on the common carotids and separated by 4 mm. The average magnetization over the common carotid cross section was determined from the intravascular signal in three coronal spoiled gradient-echo images of the common carotids (TE = 5.75 ms, TR = 200 ms, NEX = 4, 90° gaussian excitation pulse, matrix = 300 × 300, and FOV = 30 mm × 30 mm × 1 mm thick), one following regular labeling ($B_1 = 9$ μT and hard pulse of 100 ms duration), the next following sinusoidally modulation of the labeling pulse ($f_m = 400$ Hz, $B_1 = (\sqrt{2})9$ μT, and 100 ms duration) and the last by reflection of the labeling pulse ($B_1 = 9$ μT and hard pulse of 100 ms duration) about the imaging plane (to obtain equilibrium magnetization M_0). These measurements required a total of 12 min of scan time for each mouse. This protocol was adapted from an established method of measuring inversion efficiency (19).

Flow-induced adiabatic inversion in the common carotid artery was applied using a pulse with labeling time $t_L = 3.1$ s, $B_1 = 9$ μT with $G = 13$ mTm^{-1} and $f_m = 400$ Hz using the slice positioning algorithm described in the "Development of a Rapid Slice Positioning Algorithm" section. Control and label cycles were interleaved and a postlabel delay of 500 ms was applied to reduce transit time dispersion artifacts and to clear the intravascular signal (10). The whole brain was imaged using a 3D fast spin echo pulse sequence ($TE_{eff} = 4$ ms,

TR = 6.6 s, echo train length (ETL) = 12, 90° hard excitation and 180° hard refocusing pulses, 60 × 96 × 80 matrix, FOV = 60 mm × 34 mm × 28 mm, and NEX = 1) resulting in a total CASL scan time of 141 min for each of the 10 mice.

For estimating arterial transit time for use in CBF modeling, am-CASL was applied to a second batch of five C57BL/6 mice at multiple postlabel delays, namely, 50, 100, 200, 400, 800, and 1600 ms, while using a modified imaging matrix of 60 × 48 × 30 and FOV = 36 mm × 29 mm × 18 mm, resulting in a total scan time of 158 min for each mouse.

To provide reference tissue T_1 and proton density for CBF quantification, a third batch of five C57BL/6 mice were imaged using an inversion recovery pulse sequence with inversion times of 0.1, 0.3, and 2.0 s using a 2 ms hyperbolic secant inversion pulse and a 3D fast spin echo pulse sequence (TE_{eff} = 6 ms, TR = 5s, matrix = 60 × 96 × 80 with FOV = 60 mm × 34 mm × 28 mm, 90° hard excitation pulse and 180° hard refocusing pulses, ETL = 12, and NEX = 1) resulting in a total scan time of 160 min for each mouse. The T_1 and proton density maps for the five mice were registered to each other and to the control images of the am-CASL experiment, through a rigid-body landmark-matching algorithm.

Quantification and Analysis of CBF

CBF was quantified using a single-compartment biophysical model that assumes capillaries to be completely permeable to water (i.e. permeability–surface area product [*PS*] = infinity), while accounting for both transit time and MT-enhanced T_1 relaxation (10,20), namely

$$f = \frac{\lambda(S_{ctrl} - S_{lab})}{2\alpha S^0 K(\delta, w, T_{1b}, T_1, T_{1SAT})}, \quad [1]$$

where

$$K(\delta, w, T_{1b}, T_1, T_{1SAT}) = \exp\left(\frac{-\delta}{T_{1b}}\right)\exp\left(\frac{-w}{T_1}\right) \times \left[T_{1SAT}\left(1 - \exp\left(\frac{-(t_L - \delta)}{T_{1SAT}}\right)\right) - T_1\left(1 - \exp\frac{\delta}{T_1}\right)\right], \quad [2]$$

$$S^0 = \frac{1}{n}\sum_{i=1}^{n}\left(\frac{S_{ctrl}}{M_z^a(t_L + w)}\right)_i, \quad [3]$$

$$M_z^a(t_L + w) = 1 - \left(\exp\frac{-w}{T_1}\right)(1 - M_z^a(t_L)), \quad [4]$$

$$M_z^a(t_L) = \frac{p}{r}, \quad [5]$$

$$R_{1SAT} = q - \sqrt{q^2 - r}, \quad [6]$$

and where

$$p = R_b R M_0^b + R_{rfb} R_a + R_b R_a + R_a R,$$
$$q = \left(R_a + R M_0^b + R_{rfa} + R_b + R + R_{rfb}\right)/2\ , \text{ and}$$
$$r = \left(R_a + R_{rfa} + R M_0^b\right)(R_b + R_{rfb} + R) - \left(R R M_0^b\right).$$

Apart from inclusion of finite t_L, Eq. 1 is equivalent to CASL model presented by Alsop and Detre in 1996 (10), where f represents CBF, S_{ctrl} is the magnitude signal in the control image, S_{lab} is the magnitude signal in the label image, S^0 is the equilibrium tissue signal that has been corrected for MT at each voxel (Eq. 3), λ is the brain/blood partition coefficient set to equal the measured regional proton density after normalization to an average of 0.9 mL/g (21), α is measured inversion efficiency, δ is the mean value of arterial transit time as determined by curve fit in a selected region of gray matter cortex, w is the postlabel delay, and T_{1b} is the longitudinal relaxation time of blood set to 2.3 s as previously reported in rat at 7 T (22) while T_{1SAT} and T_1 refer to the longitudinal relaxation time of brain tissue with and without enhancement due to MT, respectively.

T_{1SAT} and M_a^z were calculated (Eqs. 4–6) based on a binary spin bath model of MT (8,23), using the reference T_1 maps and the known position and orientation of the labeling plane. As described in Eq. 5, the correction of S^0 for MT accounted for the postlabel delay during which no off-resonance irradiation was applied. This MT model assumed Lorentzian and superLorentzian lineshapes when computing the saturation rates, R_{rfa} and R_{rfb}, of the liquid pool A and semisolid pool B, respectively. Based on previously established curve fits of this MT model in rat temporal cortex at 4.7 T (24), this calculation used an exchange rate, R, of 12.3 Hz, a semisolid pool T_2 of 8.5 μs, a longitudinal relaxation rate of the semisolid pool, R_b, of 2.9 Hz and a semisolid pool size, M_0^b, of 0.11 which is defined relative to the normalized liquid pool size, namely, $M_0^a = 1$. The longitudinal relaxation rate of the liquid pool, R_a, was calculated as previously described (23) based on the average T_1 as measured by inversion recovery on five mice (see the "Implementation of am-CASL in Mice" section). Liquid pool T_2 was assumed to be 38.7 ms, as previously published for young mouse cortex at 7 T (25). T_{1SAT} and M_a^z were calculated by applying this MT model to the distance offset between the labeling plane of each mouse in which 3D am-CASL was performed, as shown in Fig. 1c. To assess the impact of the MT correction, CBF was calculated both with and without the use of the MT correction and the ratio was plotted, as shown in Fig. 1d.

Each CBF image was registered to the MRI anatomical brain atlas through a rigid-body landmark-matching algorithm. Mean CBF was computed in the 12 largest anatomical regions of the brain as shown in Fig. 2a–c.

To test whether there was significant regional variation in CBF, an analysis of variance (ANOVA) was performed on a linear mixed effect model of the data, with one fixed effect (region) and one random effect (specimen) using the statistical program R, available at http://www.r-project.org/. Significant regional variation in T_1 was tested using an analogous ANOVA.

To determine if CBF significantly differed between brain hemispheres, nine of the 12 brain regions were segmented into portions in each hemisphere and the mean CBF was graphically compared as illustrated in Fig. 3. An ANOVA was performed using a mixed effect linear model with hemisphere and region as fixed factors and specimen as a random factor.

A power analysis for a *t*-test was conducted (two-sided, two-sample, probability of type I error = 0.05, and

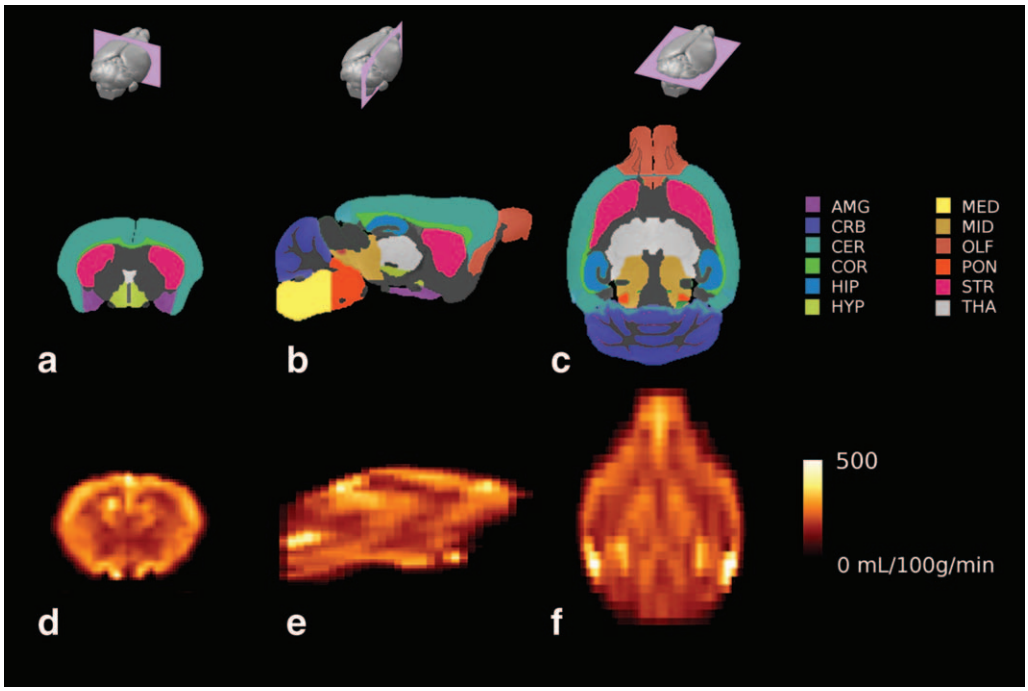

FIG. 2. Regions of interest in MRI atlas (top row) for coronal (**a**), sagittal (**b**), and transverse (**c**) images with corresponding mean CBF map (**d**, **e**, and **f**, respectively). In this figure, CBF images were interpolated by a factor of two. Legend: AMG, amygdala; CRB, cerebellar cortex; CER, cerebral cortex; COR, corpus callosum; HIP, hippocampus; HYP, hypothalamus; MED, medulla oblongata; MID, midbrain; OLF, olfactory bulbs; PON, pons; STR, striatum; and THA, thalamus.

probability of type II error = 0.2) using the measured variation in hippocampal CBF as a representative region of interest.

All computed parameters were expressed as mean ± standard-error-of-the-mean unless stated otherwise.

RESULTS

The simulation of inversion efficiency in am-CASL provided an optimized parameter set corresponding to a gradient of 13 mTm^{-1}. As illustrated in Fig. 4a, the velocity-weighted inversion efficiency peaked at B_1 = 9 μT and reached a maximum value of 0.87. The effect of varying modulation frequency, illustrated in Fig. 4b, was to increase inversion efficiency until saturation after 300 Hz. Figure 4c illustrates the dependence of longitudinal magnetization on velocity for the labeling and control experiment. Despite the oscillatory nature of the magnetization in the control experiment at high velocities and the steep drop at low velocities, there is a relatively flat region for both control and label magnetization in the range of 5 and 15 cm/s. Further, in Fig. 4d, which plots the dependence of inversion efficiency on velocity alongside a representative velocity distribution for the common carotid artery, it is apparent that the inversion efficiency is relatively constant for the velocity window that contains the bulk of the velocity distribution. This, of course, is noncoincidental as the optimized parameter set from the simulation (B_1 = 9 μT, f_m = 400 Hz, and G = 13 mTm^{-1}) were derived from the pulse-wave Doppler ultrasound measurements. Similar time averaged mean velocities were observed in all feeding arteries to the brain, with mean ± SD of 12 ± 1, 12 ± 2, 14 ± 3, 11 ± 2, 10 ± 2, 11 ± 1 cm/s for the left common carotid artery, right common carotid artery, left internal carotid artery, right internal carotid artery, left vertebral artery, and right vertebral artery, respectively.

Analysis of errors in inversion plane positioning determined that, in the event of a large variability in landmark positioning in the range of 1 mm per landmark, the mean positional and angular shifts of the inversion plane

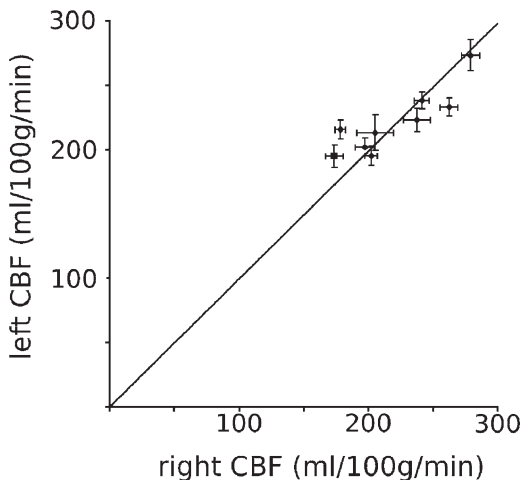

FIG. 3. Bilateral symmetry of CBF for nine brain regions (amygdala, cerebellar cortex, cerebral cortex, corpus callosum, hippocampus, hypothalamus, olfactory bulbs, striatum, and thalamus) illustrated by plotting left versus right portion of CBF. Error bars represent ± standard-error-of-the-mean for n = 10. For reference, the line of symmetry is indicated.

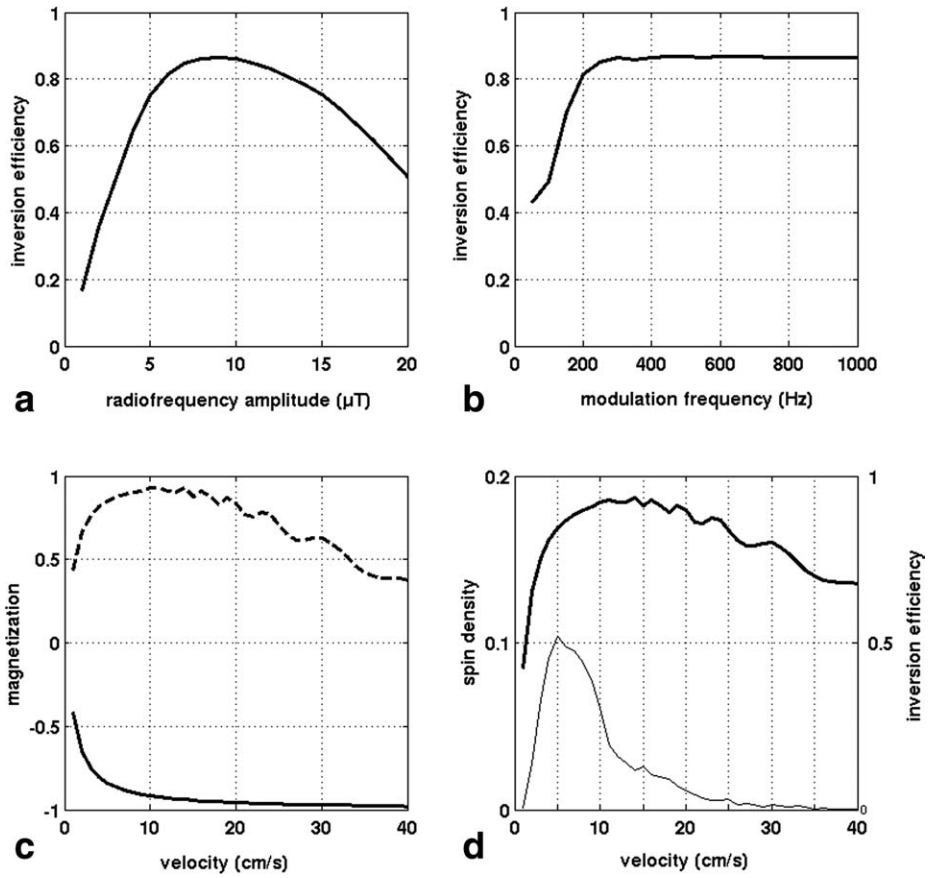

FIG. 4. **a**: Dependence of velocity-weighted inversion efficiency on B_1 for an am-CASL experiment. Simulation parameters were $G = 13$ mTm^{-1} and $f_m = 400$ Hz. Velocity-weighted inversion efficiency reaches its peak of 0.87 at $B_1 = 9$ μT. **b**: Dependence of velocity-weighted inversion efficiency on f_m for an am-CASL experiment. Simulation parameters were $G = 13$ mTm^{-1}, $B_1 = 9$ μT. **c**: Dependence of longitudinal magnetization on blood velocity for control pulse (dashed curve) and labeling pulse (solid curve) in an am-CASL experiment with $G = 13$ mTm^{-1}, $B_1 = 9$ μT, and $f_m = 400$ Hz. **d**: Dependence of inversion efficiency (thick curve) on blood velocity. Blood velocity distribution is also shown (thin curve). Simulation parameters were $G = 13$ mTm^{-1}, $B_1 = 9$ μT, and $f_m = 400$ Hz.

were 2.4 mm and 18.6°, respectively. Misalignment of this magnitude would result in an inversion efficiency loss of 0.5%. The selected vascular landmarks, based on micro-CT images, were found to have low intermouse variation (SD 0.19 mm).

Statistically significant differences in CBF [$F(11,99) = 19.28$, $P < 0.0001$] and T_1 [$F(11,44) = 176.31$, $P < 0.0001$] were observed over the 12 regions examined, with values listed in Table 1. T_1 for the total brain was 1.53 ± 0.01 s. Based on the MT model, the group average T_{1SAT} and $M_z^a(t_L + w)$ were 0.57 s and 0.48, respectively. CBF for brain was found to be 219 ± 6 mL/100 g/min, based on the measured inversion efficiency of 0.67 ± 0.03 and the fitted arterial transit time of 0.08 ± 0.02 s. In comparison, CBF calculated without MT correction was 217 ± 5 mL/100 g/min. As summarized in Table 1 and Fig. 1d, accounting for MT led to notable increases in CBF in caudal regions of the brain, while CBF in rostral regions decreased due to MT correction. Maps of mean CBF with the corresponding regions of interest are shown for coronal, sagittal, and transverse views in Fig. 2. CBF was found to be highly symmetric bilaterally and there was no significant hemispheric difference in CBF [$F(1,153) = 0.12$, $P = 0.73$]. The bilateral symmetry of volumetric CBF measurements is displayed in Fig. 3. Based on the power analysis, displayed in Fig. 5, CBF differences as low as 10% should be statistically significant for studies conducted with 12 animals per group.

DISCUSSION

Selecting a mouse ASL protocol involves making a series of choices: first, the protocol for spatially selective labeling can either be pulsed ASL, where blood water magnetization is labeled in a large slab proximal to the imaging slice, or CASL, where blood water magnetization is continuously labeled as it flows through a plane intersecting the carotid arteries. CASL was selected for this

Table 1
Regional Values (Mean ± Standard-Error-of-the-Mean) of T_1 ($n = 5$) and CBF ($n = 10$)

Brain region	T_1 (s)	CBF (mL/100 g/min) uncorrected for MT	CBF (mL/100 g/min) corrected for MT
Amygdala	1.65 ± 0.03	176 ± 7	183 ± 7
Cerebellar cortex	1.50 ± 0.02	187 ± 12	209 ± 13
Cerebral cortex	1.59 ± 0.01	240 ± 6	240 ± 6
Corpus callosum	1.54 ± 0.01	202 ± 6	199 ± 5
Hippocampus	1.55 ± 0.01	273 ± 7	277 ± 7
Hypothalamus	1.50 ± 0.01	228 ± 9	231 ± 9
Medulla	1.33 ± 0.01	175 ± 13	203 ± 15
Midbrain	1.33 ± 0.01	189 ± 10	189 ± 10
Olfactory bulbs	1.61 ± 0.01	258 ± 7	247 ± 6
Pons	1.38 ± 0.02	190 ± 11	201 ± 12
Striatum	1.63 ± 0.01	190 ± 5	189 ± 5
Thalamus	1.45 ± 0.01	202 ± 7	199 ± 7

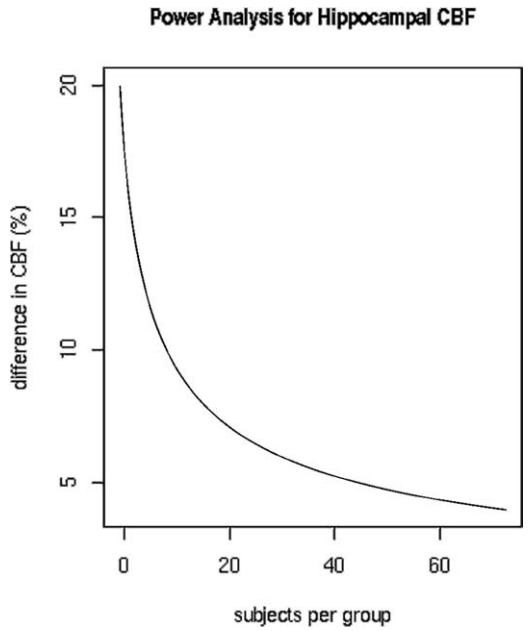

FIG. 5. Power analysis (two-sample, two-sided, probability of type I error = 0.05, and probability of type II error = 0.2) for difference in hippocampal CBF.

work due to its inherently higher signal strength (26). Second, an image readout portion of the protocol must be selected. This article focused on a 3D approach to ASL. By imaging the entire brain, one can screen mutant mice for regional CBF phenotypes, while permitting regions of interest to be defined retrospectively. Relative to single slice imaging, whole brain imaging also facilitated automated registration to an MRI atlas and subsequent data mining. Furthermore, 3D imaging has the advantage that overlap of slice excitation profiles and saturation of arterial blood by proximal slice excitation can be avoided. Third, a choice must be made between implementing CASL using a separate coil for labeling or using only the imaging coil (27). Single-coil CASL was implemented to avoid the need for additional hardware. This choice forces one to choose a strategy to control for MT. This article used the am-CASL labeling protocol (28), which places lower demands on the MRI gradient than pseudo-continuous ASL while maintaining high inversion efficiency (29). Moreover, relative to the simultaneous proximal and distal irradiation method, am-CASL provides more consistent control of MT effects over the entire brain (30).

A slice positioning algorithm was developed to position the labeling plane perpendicular to the common carotid arteries to ensure that the apparent velocity through the plane is high enough to avoid inefficiency associated with low velocity. In the mouse, this slice positioning algorithm is robust, as demonstrated by the simulated reduction of only 0.5 in inversion efficiency associated with the hypothetical case of large variability in landmark selection. Furthermore, this method is easy to implement when labeling blood in the long and parallel common carotid arteries. By using the inversion plane position recommended in this article, comparable inversion efficiency is expected for the vertebral and common carotid arteries, given their similar orientation and velocity distribution. Variation in neck posture between micro-CT and MRI scans was reduced by the use of an anatomically molded sled during MRI scanning and by careful positioning during fixation in the previous micro-CT study. Observed variation in the angulation of the common carotids among micro-CT specimens was $\sim 10^{\circ}$, suggesting that any systematic effect of postural differences on inversion efficiency was small compared to other factors. Labeling of the common carotid arteries is preferable to the internal carotid arteries, as MT enhancement of T_1 in the vicinity of the labeling plane will reduce the magnitude of the difference signal and, hence, reduce the precision of the CBF estimate.

Pulsed Doppler ultrasound measurements provide an efficient method to characterize common carotid blood velocity in mice. Furthermore, the calculated inversion parameters were robust with respect to blood velocity variation. This suggests that remeasurement of blood velocity should only be necessary in cases where very large changes in carotid velocity are expected (e.g. a stroke model) or measured inversion efficiency is suboptimal. Although the difference between measured and simulated inversion efficiency may be partly explained based on the known bias in favor of measuring slower moving spins (31), another potential factor is T_{2b}. There is considerable variation in the literature on measured T_{2b} (17,32–34), which is likely related to both physiological factors such as oxygenation and hematocrit as well as the timescale over which refocusing occurs. Short refocusing intervals lead to significantly larger T_{2b} estimates (35). The relatively rapid transition that occurs during am-CASL inversion can be treated as a short refocusing period and justifies the use of longer T_{2b} values when calculating inversion efficiency. For comparison, inversion efficiency for a shorter T_{2b} of 70 ms was estimated at 0.64 when compared with 0.87 with a T_{2b} of 250 ms. A benefit of using measured inversion efficiency in calculations of CBF is to reduce variability due to individual velocity differences. Although the mean velocity as measured by ultrasound was consistent across the group, it is still possible to find individual mice with atypical velocity distributions, which can ultimately impact inversion efficiency.

As depicted in Fig. 2d–f, the described 141-min CASL protocol provided high enough SNR to reveal blood flow contrast between neighboring brain structures such as the cerebral cortex and surrounding white matter. Based on recorded heart rate, respiration, and temperature, physiological parameters were stable throughout each CASL scan. This is consistent with a previous study that found that under similar anesthesia conditions, CBF was stable over 70 min (36). Where necessary it should be possible to reduce scan times by using a shorter labeling period, leading to lower SNR. The reduced SNR may, however, increase variability in the CBF data, which may in turn compromise statistical power. Additional SNR could be gained by reducing postlabel delay to significantly less than 500 ms, which was an overly conservative selection given that the measured arterial transit time was only 80 ms.

As shown in Table 1, the observed regional CBF values were larger in gray than white matter structures. Brain stem structures such as the medulla, pons, and midbrain, which have a mixture of gray and white matter, tended to have only slightly lower CBF than major gray matter regions such as the cerebral cortex. A diverse range of CBF values in mice have been reported under similar experimental conditions. For example, three single-coil CASL studies on horizontally loaded mice maintained at 37°C and anesthetized with average isoflurane concentration (mean ± SD) of 1.3 ± 0.6%, reported whole brain CBF (mean ± SD) of 208 ± 12 mL/100 g/min (37), 215 ± 27 mL/100 g/min (5), and 165 ± 13 mL/100 g/min (4). The whole brain MT-corrected CBF (mean ± SD) reported in this study of 219 ± 18 mL/100 g/min, whereas similar to other single-coil CASL studies, is higher than that reported by autoradiography (38,39). Although the explanation for this difference between autoradiography and CASL is presently unclear, a similar discrepancy has been previously reported for single-coil CASL studies applied to the rat brain (40). Differences in body temperature (36), anesthesia level (41), and subject orientation (5) may account for some of the reported differences in CBF.

The need to account for MT enhancement of T_1 could be avoided by using a much higher gradient (>200 mTm^{-1}) or much lower B_1. The former option is, however, challenging due to hardware overheating limits, whereas the later option may restrict the inversion efficiency to impractically low values. In this study, CBF was modeled to account for MT effects, which has not been routinely applied in mouse ASL studies. Although local CBF values were affected by the MT correction, the relatively minor global effect of the correction may partly explain why this effect has been underreported in past mouse ASL studies. As shown in Fig. 1d and tabulated in Table 1, the observed pattern of variation of the MT effect on CBF is dependent on position and orientation of the labeling plane. MT effects were accounted for in the CBF modeling to avoid having to measure this effect for each mouse. To improve accuracy of MT modeling, this study used T_1 and T_2 of the liquid pool based on mouse brain data at 7 T. Four parameters in the binary spin bath model were based on 4.7-T rat brain data, namely, exchange rate, semisolid pool size, semisolid pool T_1, and semisolid pool T_2. The accuracy of this extrapolation of MT parameters to 50% higher field strength is supported by a study that compared these MT parameters over a wider field strength range in three concentrations of agar and reported little variation (23). Furthermore, CBF as computed by Eq. 1 was found to be relatively insensitive to substantial variations in those MT parameters that were adopted from 4.7 T. It is, however, possible that direct measurement of T_{1SAT} and the equilibrium tissue signal may further refine CBF modeling (9,42).

Two-compartment CBF models have been proposed as an enhancement for human ASL. The single-compartment model applied in this study assumes complete permeability of the capillary wall to water exchange (i.e. PS = infinity). Applying the two-compartment model, namely, the fast flow solution proposed by Parkes and Tofts (43), to data in this study using a PS reported for rat cerebral cortex of 3.3 mL/(g min) (44), a blood volume of 0.04 (45) and a blood water content of 0.7 (46), provided a whole brain CBF estimate of 221 mL/100 g/min, which is within 1% of the value computed using the single-compartment model. In fact, the single- and two-compartment models differed by less than 10% provided that PS was selected to be more than 1.7 mL/(g min). This suggests that the single-compartment model is realistic for use in computing mouse brain CBF.

The development of robust am-CASL in mice was motivated by a desire to pursue large-scale applications that would greatly benefit from high-throughput protocols. As demonstrated by the power analysis, it is feasible to detect small differences in CBF when screening moderate numbers of mutant mice.

ACKNOWLEDGMENTS

The authors thank Willem van Heiningen for his support and advice on the MRI component of this study and Lisa Yu for her assistance with micro-CT imaging.

REFERENCES

1. Leithner C, Gertz K, Schröck H, Priller J, Prass K, Steinbrink J, Villringer A, Endres M, Lindauer U, Dirnagl U, Royl G. A flow sensitive alternating inversion recovery (FAIR)-MRI protocol to measure hemispheric cerebral blood flow in a mouse stroke model. Exp Neurol 2008;210:118–127.
2. Kennan RP, Machado FS, Lee SC, Desruisseaux MS, Wittner M, Tsuji M, Tanowitz HB. Reduced cerebral blood flow and *N*-acetyl aspartate in a murine model of cerebral malaria. Parasitol Res 2005;96: 302–307.
3. Kennan RP, Suzuka SM, Nagel RL, Fabry ME. Decreased cerebral perfusion correlates with increased BOLD hyperoxia response in transgenic mouse models of sickle cell disease. Magn Reson Med 2004;51:525–532.
4. Weidensteiner C, Metzger F, Bruns A, Bohrmann B, Kuennecke B, von Kienlin M. Cortical hypoperfusion in the B6.PS2APP mouse model for Alzheimer's disease: comprehensive phenotyping of vascular and tissular parameters by MRI. Magn Reson Med 2009;62:35–45.
5. Foley LM, Hitchens TK, Kochanek PM, Melick JA, Jackson EK, Ho C. Murine orthostatic response during prolonged vertical studies: effect on cerebral blood flow measured by arterial spin-labeled MRI. Magn Reson Med 2005;54:798–806.
6. Werner R, Norris DG, Alfke K, Mehdorn HM, Jansen O. Improving the amplitude-modulated control experiment for multislice continuous arterial spin labeling. Magn Reson Med 2005;53:1096–1102.
7. O'Gorman RL, Summers PE, Zelaya FO, Williams SCR, Alsop DC, Lythgoe DJ. In vivo estimation of the flow-driven adiabatic inversion efficiency for continuous arterial spin labeling: a method using phase contrast magnetic resonance angiography. Magn Reson Med 2006;55: 1291–1297.
8. Morrison C, Henkelman RM. A model for magnetization transfer in tissues. Magn Reson Med 1995;33:475–482.
9. Ewing JR, Cao Y, Fenstermacher J. Single-coil arterial spin-tagging for estimating cerebral blood flow as viewed from the capillary: relative contributions of intra- and extravascular signal. Magn Reson Med 2001;46:465–475.
10. Alsop DC, Detre JA. Reduced transit-time sensitivity in noninvasive magnetic resonance imaging of human cerebral blood flow. J Cereb Blood Flow Metab 1996;16:1236–1249.
11. Dorr AE, Lerch JP, Spring S, Kabani N, Henkelman RM. High resolution three-dimensional brain atlas using an average magnetic resonance image of 40 adult C57Bl/6J mice. Neuroimage 2008;42:60–69.
12. Spring S, Lerch JP, Henkelman RM. Sexual dimorphism revealed in the structure of the mouse brain using three-dimensional magnetic resonance imaging. Neuroimage 2007;35:1424–1433.
13. Chugh BP, Lerch JP, Yu LX, Pienkowski M, Harrison RV, Henkelman RM, Sled JG. Measurement of cerebral blood volume in mouse brain

regions using micro-computed tomography. Neuroimage 2009;47: 1312–1318.
14. Fridman Y, Pizer SM, Aylward S, Bullitt E. Extracting branching tubular object geometry via cores. Med Image Anal 2004;8:169–176.
15. Sibson R. Studies in the robustness of multidimensional scaling: Procrustes statistics. J R Stat Soc 1978;40:234–238.
16. Zhou YQ, Foster FS, Nieman BJ, Davidson L, Chen XJ, Henkelman RM. Comprehensive transthoracic cardiac imaging in mice using ultrasound biomicroscopy with anatomical confirmation by magnetic resonance imaging. Physiol Genomics 2004;18:232–244.
17. Stanisz GJ, Odrobina EE, Pun J, Escaravage M, Graham SJ, Bronskill MJ, Henkelman RM. T_1, T_2 relaxation and magnetization transfer in tissue at 3 T. Magn Reson Med 2005;54:507–512.
18. Dazai J, Bock NA, Nieman BJ, Davidson LM, Henkelman RM, Chen XJ. Multiple mouse biological loading and monitoring system for MRI. Magn Reson Med 2004;52:709–715.
19. Zhang W, Williams DS, Koretsky AP. Measurement of rat brain perfusion by NMR using spin labeling of arterial water: in vivo determination of the degree of spin labeling. Magn Reson Med 1993;29: 416–421.
20. Thomas DL, Lythgoe MF, van der Weerd L, Ordidge RJ, Gadian DG. Regional variation of cerebral blood flow and arterial transit time in the normal and hypoperfused rat brain measured using continuous arterial spin labeling MRI. J Cereb Blood Flow Metab 2005;26: 274–282.
21. Roberts DA, Rizi R, Lenkinski RE, Leigh JS. Magnetic resonance imaging of the brain: blood partition coefficient for water: application to spin-tagging measurement of perfusion. J Magn Reson Imaging 1996;6:363–366.
22. Barbier EL, Grillon E, D'corps M. In-vivo T_1 measurements in the rat brain accounting for inflow effects. In: Proceedings of the Eighth Annual Meeting ISMRM, Denver, Colorado, 2000. p 165.
23. Henkelman RM, Huang X, Xiang QS, Stanisz GJ, Swanson SD, Bronskill MJ. Quantitative interpretation of magnetization transfer. Magn Reson Med 1993;29:759–766.
24. Quesson B, Thiaudière E, Delalande C, Dousset V, Chateil JF, Canioni P. Magnetization transfer imaging in vivo of the rat brain at 4.7 T: interpretation using a binary spin-bath model with a superLorentzian lineshape. Magn Reson Med 1997;38:974–980.
25. Guilfoyle DN, Dyakin VV, O'Shea J, Pell GS, Helpern JA. Quantitative measurements of proton spin-lattice (T_1) and spin–spin (T_2) relaxation times in the mouse brain at 7.0 T. Magn Reson Med 2003; 49:576–580.
26. Wang J, Zhang Y, Wolf RL, Roc AC, Alsop DC, Detre JA. Amplitude-modulated continuous arterial spin-labeling 3.0-T perfusion MR imaging with a single coil: feasibility study. Radiology 2005;235: 218–228.
27. Muir ER, Shen Q, Duong TQ. Cerebral blood flow MRI in mice using the cardiac-spin-labeling technique. Magn Reson Med 2008;60: 744–748.
28. Alsop DC, Detre JA. Multisection cerebral blood flow MR imaging with continuous arterial spin labeling. Radiology 1998;208:410–416.
29. Pohmann R, Budde J, Auerbach EJ, Adriany G, Uğurbil K. Theoretical and experimental evaluation of continuous arterial spin labeling techniques. Magn Reson Med 2010;63:438–446.
30. Barbier EL, Lamalle L, Décorps M. Methodology of brain perfusion imaging. J Magn Reson Imaging 2001;13:496–520.
31. Maccotta L, Detre JA, Alsop DC. The efficiency of adiabatic inversion for perfusion imaging by arterial spin labeling. NMR Biomed 1997; 10:216–221.
32. Wright GA, Hu BS, Macovski A. Estimating oxygen saturation of blood in vivo with MR imaging at 1.5 T. J Magn Reson Imaging 1991; 1:275–283.
33. Chen JJ, Pike GB. Human whole blood T_2 relaxometry at 3 Tesla. Magn Reson Med 2009;61:249–254.
34. Gardener AG, Francis ST, Prior M, Peters A, Gowland PA. Dependence of blood R_2 relaxivity on CPMG echo-spacing at 2.35 and 7 T. Magn Reson Med 2010;64:967–974.
35. Stefanovic B, Pike GB. Human whole-blood relaxometry at 1.5 T: assessment of diffusion and exchange models. Magn Reson Med 2004;52:716–723.
36. Zheng B, Lee PTH, Golay X. High-sensitivity cerebral perfusion mapping in mice by kbGRASE-FAIR at 9.4 T. NMR Biomed 2010;23: 1061–1070.
37. Sun Y, Schmidt NO, Schmidt K, Doshi S, Rubin JB, Mulkern RV, Carroll R, Ziu M, Erkmen K, Poussaint TY, Black P, Albert M, Burstein D, Kieran MW. Perfusion MRI of U87 brain tumors in a mouse model. Magn Reson Med 2004;51:893–899.
38. Jay TM, Lucignani G, Crane AM, Jehle J, Sokoloff L. Measurement of local cerebral blood flow with [14C]iodoantipyrine in the mouse. J Cereb Blood Flow Metab 1988;8:121–129.
39. Maeda K, Mies G, Oláh L, Hossmann KA. Quantitative measurement of local cerebral blood flow in the anesthetized mouse using intraperitoneal [14C]iodoantipyrine injection and final arterial heart blood sampling. J Cereb Blood Flow Metab 2000;20:10–14.
40. Ewing JR, Cao Y, Knight RA, Fenstermacher JD. Arterial spin labeling: validity testing and comparison studies. J Magn Reson Imaging 2005;22:737–740.
41. Hendrich KS, Kochanek PM, Melick JA, Schiding JK, Statler KD, Williams DS, Marion DW, Ho C. Cerebral perfusion during anesthesia with fentanyl, isoflurane, or pentobarbital in normal rats studied by arterial spin-labeled MRI. Magn Reson Med 2001;46:202–206.
42. Ewing JR, Jiang Q, Boska M, Zhang ZG, Brown SL, Li GH, Divine GW, Chopp M. T_1 and magnetization transfer at 7 Tesla in acute ischemic infarct in the rat. Magn Reson Med 1999;41:696–705.
43. Parkes LM, Tofts PS. Improved accuracy of human cerebral blood perfusion measurements using arterial spin labeling: accounting for capillary water permeability. Magn Reson Med 2002;48:27–41.
44. Schwarzbauer C, Morrissey SP, Deichmann R, Hillenbrand C, Syha J, Adolf H, Nöth U, Haase A. Quantitative magnetic resonance imaging of capillary water permeability and regional blood volume with an intravascular MR contrast agent. Magn Reson Med 1997;37:769–777.
45. Edvinsson L, Nielsen KC, Owman C. Circadian rhythm in cerebral blood volume of mouse. Experientia 1973;29:432–433.
46. Nakagawa H, Lin S, Bereczki D, Gesztelyi G, Otsuka T, Wei L, Hans F, Acuff V, Chen J, Pettigrew K, Patlak C, Blasberg R, Fenstermacher J. Blood volumes, hematocrits, and transit-times in parenchymal microvascular systems of the rat brain. In: Le Bihan D, editor. Diffusion and perfusion magnetic resonance imaging. New York: Raven Press; 1995. pp 193–200.